Thermal and Mechanical Analyses of Compliant Thermoelectric Coils for Flexible and Bio-integrated Devices

Kan Li
Department of Engineering
University of Cambridge
Cambridge CB2 1PZ, UK
Email: kl513@cam.ac.uk

Lin Chen
State Key Laboratory for Mechanical
Behavior of Materials,
School of Materials Science and Engineering,
Xi'an Jiaotong University
Xi'an, Shaanxi 710000, P. R. China
Email: chenlinxjtu@163.com

Feng Zhu
School of Logistics Engineering
Wuhan University of Technology
Wuhan, Hubei 430063, P. R. China
Email: zhufeng@whut.edu.cn

Yonggang Huang*
Departments of Civil and Environmental Engineering,
Mechanical Engineering, and
Materials Science and Engineering
Center for Bio-Integrated Electronics
Northwestern University
Evanston, IL 60208
Email: y-huang@northwestern.edu

Three-dimensional coil structures assembled by mechanically guided compressive buckling have shown potential in enabling efficient thermal impedance matching of thermoelectric devices at a small characteristic scale, which increases the efficiency of power conversion, and has the potential to supply electric power to flexible bio-integrated devices. The unconventional heat dissipation behavior at the side surfaces of the thin-film coil, which serves as a 'heat pump', is strongly dependent on the geometry and the material of the encapsulating dissipation layer (e.g., polyimide). The low heat transfer coefficient of the encapsulation layer, which may damp the heat transfer for a conventional thermoelectric device, usually limits the heat transfer efficiency. However, the unconventional geometry of the coil can take advantage of the low heat transfer coefficient to increase its hot-to-cold temperature difference, and this requires further thermal analysis of the coil in order to improve its power conversion efficiency. Another challenge for the coil is that the active thin-film thermoelectric materials employed (e.g., heavily doped Silicon) are usually very brittle, with the fracture strain less than 0.1% in general while the overall device may undergo large deformation (e.g., stretched 100%). Mechanical analysis is therefore necessary to avoid failure/fracture of the thermoelectric material. In this work, we study the effect of coil geometry on both thermal and mechanical behaviors by using numerical and analytical approaches, and optimize the coil geometry to improve the de-

*Corresponding author

vice performance, and to guide its design for future applications.

Keywords: compliant coil, thin-film thermoelectric material, mechanical analysis, thermal analysis

1 Introduction

The growing interest of 3D (three-dimensional) mesostructures of functional materials attributes to their utility in a range of areas, such as energy storage and generation devices [1–3], mechanical and optical meta materials [4–6], stretchable electronics [7–10], and biomedical devices [11–13]. Many recent works have reported methods for forming such 3D configurations including 3D printing [14–16], thin-film folding and winkling [17–19], and actuation of active materials [20–22]. A collection of recent works [23–32] exploit a new strategy, i.e., buckling-guided 3D assembly that forms the 3D mesostructures by the compressive buckling of 2D precursors selectively bonded onto prestretched elastomer substrates. This assembly technique is intrinsically compatible with the planar technologies for a wide range of classes of functional materials, including device-grade semiconductors, and has some attractive features such as parallel operation, high speed, and size scalability, ranging from nanometers to centimeters [33–40]. These capabilities provide more design spaces for this assembly technique, and demonstrate a promising future for practical applications.

Thermoelectric devices generate electrical power from heat flux utilizing thermal gradients, which are ubiquitous [41]. For miniature wearable devices, it is promising to use the temperature difference between the human body and the environment to provide the required small-scale amounts of power. A key challenge is to match the thermal impedance of heat exchange in the natural direction of the heat flow, which is typically oriented out of the plane through the device. Using thick thermoelectric material films (tens to hundreds of micrometers) can help match the out-of-plane impedance, but the resulting devices are usually bulky. Additionally, the heat exchange capabilities from natural air convection in such thick-material devices are limited by their planar surface areas. The use of thin-film thermoelectric materials is promising to over these challenges, benefitting from the large surface area to enhance the air convection, with their in-plane direction oriented to the direction of the heat flow to match the thermal impedance of heat exchange.

By use of thin-film thermoelectric materials with the buckling-guided 3D assembly, Nan et al. [42] designed a new thin-film thermoelectric coil. The 3D configuration allows the thin-film thermoelectric material to generate voltage drop from the temperature gradient that forms in the film plane, and to conduct heat exchange between environment and the device via natural air convection throughout its large surface area. In addition, this thermoelectric coil has mechanical compliance and large stretchability ($> 60\%$), and can serve as the basic component of a flexible thermoelectric generator to supply electrical power for miniature flexible devices. However, the achieved power output of this thermoelectric coil was very low (i.e., ≈ 0.03nW per coil). On one hand, the low figure of merit ZT of silicon ($ZT > 10^{-3}$ at 300K) limits the power output. Replacing the active thermoelectric material with those of better ZT, i.e., Bi_2Te_3-Sb_2Te_3 with $ZT > 0.1$, can significantly increase the power. On the other hand, the influence of the geometric parameters of the coils are only modestly studied. There is room for significant increase of power output by optimizing the key geometric parameters of the coil via analytically modelling. Moreover, due to the low fracture strain ($< 0.1\%$) of the doped silicon [43], it is important to optimize the geometric parameters in order to reduce the maximum strain in the coil, therefore to achieve large stretchability of the device.

This paper provides the thermal and mechanical analyses of compliant thermoelectric coils in order to increase its efficiency of power generation, and to improve the mechanical robustness (i.e., to ensure that the brittle thermoelectric material does not fracture). We study the effect of the geometric parameters of coils on the heat transfer behavior and the maximum strain in the silicon layer, by finite element analysis (FEA) and analytical models, taking the highly doped silicon (Si) for the functional thermoelectric material and polyimide (PI) for the material of encapsulating layer as a representative example. Further optimizations are performed based on these results to maximize the thermal-to-electric power and minimize the maximum strain in the thermoelectric material.

2 Results

2.1 Thermal Analysis

The 3D configuration of the coil is formed by a 2-step process, as shown in Fig. 1. The 2D precursor is selectively bonded onto a prestretched elastomer substrate (e.g., prestrain $\varepsilon_{\text{pre}} = 100\%$) at the bonding sites. The 2D precursor buckles to form the 3D configuration upon release of the prestretch in the substrate (see Fig. 1a). The 2D precursor is a thin film (ribbon) composed of 2 semicircles of mid-axial radius R in the plane. Its cross section shows the Si layer sandwiched by PI layers to protect Si. The geometric parameters of the thin film have the baseline values: radius $R = 400\mu$m, width $w_{\text{PI}} = 120\mu$m and $w_{\text{Si}} = 60\mu$m, and thickness $t_{\text{PI}} = 2\mu$m and $t_{\text{Si}} = 0.2\mu$m. Each parameter may deviate from its baseline value in the following parametric studies.

Figure 2 presents the analytical model for heat transfer in the coil. The 3D configuration of the coil (shown in Fig. 2a) is inherently different from the conventional thermoelectric devices. Figure 2b shows a conventional thermoelectric device, in which the heat flux from the hot side goes through the thermoelectric legs to the cold side, without any dissipation in the thermoelectric legs. However, for the coils, part of the heat dissipates into the air through the PI-air interface because the thermoelectric coil utilize the PI as the "heat sink" to cool down, and this dissipation helps to promote heat transfer between the substrate (hot side) and the air (cold side). The convective heat dissipation $\mathrm{d}\dot{Q}_{\text{diss}} = \alpha(T - T_{\text{env}})\ell w_{\text{PI}} \mathrm{d}\zeta$ applies at the PI-air interface for both sides of the thin film (ribbon), where T is the local temperature in the ribbon, $T_{\rm env}$ is the environmental temperature, $\alpha = 5.0\mathrm{W}/(\mathrm{m}^2\cdot\mathrm{K})$ is the convection coefficient, $\ell = 2\pi R$ is the length of the thermoelectric leg, and $\zeta \in [0,1]$ is the normalized position on the thermoelectric leg, with $\zeta = 0$ and 1 denote the substrate (hot side) and air (cold side), respectively. Heat transfer in a thin-film coil can be simplified as a one-dimensional problem (along the ribbon length), as shown in Fig. 2c, because the length ℓ of a coil leg is much larger than its width and thickness. The conservation of energy requires

$$\frac{\mathrm{d}\dot{Q}}{\mathrm{d}\zeta} = -2\frac{\mathrm{d}\dot{Q}_{\rm diss}}{\mathrm{d}\zeta} = -2\alpha(T - T_{\rm env})\ell w_{\rm PI}, \tag{1}$$

where $\dot{Q}$ is the local heat flux, and it is related to negative gradient of the temperature based on the Fourier's law of heat conduction

$$\dot{Q} = -\left(k_{\rm PI}w_{\rm PI}t_{\rm PI} + k_{\rm Si}w_{\rm Si}t_{\rm Si}\right)\frac{1}{\ell}\frac{\mathrm{d}T}{\mathrm{d}\zeta}, \tag{2}$$

where $k_{\rm PI} = 0.46\mathrm{W}/(\mathrm{m}\cdot\mathrm{K})$ and $k_{\rm Si} = 80\mathrm{W}/(\mathrm{m}\cdot\mathrm{K})$ are the heat transfer coefficients for PI and Si, respectively. The boundary conditions are zero heat flux $\dot{Q}|_{\zeta=1} = 0$ at the cold side, and a constant temperature $T|_{\zeta=0} = T_{\rm h}$, where $T_{\rm h}$ represents the temperature of human body. In the following we consider a constant width and a (linearly) gradient width of the PI layer.

2.1.1 Coils of Constant Width

For the simplest case that the ribbon has a constant width $w_{\rm PI}$ along its length (and also constant $t_{\rm PI}$, $w_{\rm Si}$ and $t_{\rm Si}$), Eqs. (1) and (2), together with the boundary conditions above, have the solution

$$\frac{T_{\rm h} - T}{T_{\rm h} - T_{\rm env}} = 1 - \frac{\cosh[\beta(1-\zeta)]}{\cosh(\beta)}, \tag{3}$$

where $\beta = \ell/\ell_{\rm c}$ is the normalized length of the ribbon, and $\ell_{\rm c} = \sqrt{\frac{k_{\rm PI}w_{\rm PI}t_{\rm PI}+k_{\rm Si}w_{\rm Si}t_{\rm Si}}{2\alpha w_{\rm PI}}}$ is a characteristic length, and $\ell_{\rm c} \approx 0.94$ mm for the baseline values. Figure 3a shows that the temperature distribution in Eq. (3) agrees very well with the numerical solution obtained by FEA, which is fully 3D and accounts for all details of the geometry, without any parameter meeting. The commercial FEA software ABAQUS is used, with the coil modeled by a 3-layer (PI-Si-PI) composite. The 4-node heat transfer quadrilateral shell elements are employed, with at least 8 elements along the width to ensure accuracy.

Equation (3) gives the hottest-to-coldest temperature drop ΔT as

$$\frac{\Delta T}{T_{\rm h} - T_{\rm env}} = 1 - \frac{1}{\cosh(\beta)}. \tag{4}$$

The maximum possible power output of a single thermoelectric coil is reached when the electric impedance of the load $Z_{\rm load}$ equals that of the source ($Z_{\rm coil}$ for the coil), i.e., $Z_{\rm load} = Z_{\rm coil} = 2\ell/(\sigma w_{\rm Si}t_{\rm Si})$. The maximum power is then derived from the thermoelectric voltage $\Delta V = 2S_{\rm Si}\Delta T$ of the coil as

$$\begin{aligned} P_{\rm m} &= \frac{1}{2}\frac{\Delta V^2}{Z_{\rm load}+Z_{\rm coil}} \\ &= \frac{1}{2}S_{\rm Si}^2\sigma w_{\rm Si}t_{\rm Si}\cdot\frac{\Delta T^2}{\ell} \\ &= \frac{1}{2}ZT_{\rm h}\cdot\left(1-\frac{T_{\rm env}}{T_{\rm h}}\right)^2\cdot LT_{\rm h}. \end{aligned} \tag{5}$$

Here, $ZT_{\rm h} = T_{\rm h}\cdot\frac{\sigma S_{\rm Si}^2}{k_{\rm Si}}$ is the thermoelectric figure of merit for Si, σ and $S_{\rm Si} = 0.92\mathrm{mV/K}$ are the electrical conductivity and the (temperature-independent) Seebeck coefficient of Si, respectively; and $LT_{\rm h}$ is the power transfer factor

$$\begin{aligned} LT_{\rm h} &\equiv T_{\rm h}\cdot k_{\rm Si}w_{\rm Si}t_{\rm Si}\frac{1}{\ell}\left(\frac{\Delta T}{T_{\rm h}-T_{\rm env}}\right)^2 \\ &= T_{\rm h}\cdot\frac{k_{\rm Si}w_{\rm Si}t_{\rm Si}}{\ell_{\rm c}}\cdot\frac{1}{\beta}\left[1-\frac{1}{\cosh(\beta)}\right]^2, \end{aligned} \tag{6}$$

which characterizes the effect of geometry on the power output of a coil.

Even though the hottest-to-coldest temperature drop ΔT in Eq. (4) increases monotonously with the normalized length β, the power output coefficient $LT_{\rm h}$ reaches a maximum when $\beta = 2.45$ (or $\ell = 2.45\ell_{\rm c}$), as shown in Fig. 3b. Its after-peak decrease results from the increase of the electrical impedance of the coil. This maximum $LT_{\rm h}$ is

$$\max(LT_{\rm h}) \approx 0.28\cdot T_{\rm h}\cdot\frac{k_{\rm Si}w_{\rm Si}t_{\rm Si}}{\ell_{\rm c}}, \tag{7}$$

which gives 83.4μW for the baseline values. Its substitution into Eq. (5) gives the maximum power output of 0.16nW for a single coil (at the baseline values) with the estimated figure of merit of Si $ZT_{\rm h} \approx 10^{-3}$. This power is more than 5 times larger than the previous work (0.03nW) [42], illustrating the advantage of coil design for thermoelectric devices.

2.1.2 Coils of Gradient PI Width

In order to further increase the power output, we study coils with the gradient PI width, which varies linearly along the length (see Fig. 4),

$$w_{\rm PI} = w_0\cdot(1+B\zeta), \tag{8}$$

where w_0 and $w_0(1+B)$ are the widths at the hot and cold sides, respectively. The other width and thickness $t_{\rm PI}$, $w_{\rm Si}$

and t_{Si} are still constant. Equations (1) and (2) become

$$\frac{\mathrm{d}\dot{Q}}{\mathrm{d}\zeta} = -\frac{\mathrm{d}\dot{Q}_{\text{diss}}}{\mathrm{d}\zeta} = -2\alpha(T - T_{\text{env}})\ell w_0 \cdot (1 + B\zeta) \tag{9}$$

and

$$\dot{Q} = -\left[k_{\text{PI}} w_0 t_{\text{PI}} \cdot (1 + B\zeta) + k_{\text{Si}} w_{\text{Si}} t_{\text{Si}}\right] \frac{1}{\ell} \frac{dT}{d\zeta}. \tag{10}$$

Subtitution of Eq. (10) into Eq. (9) gives

$$\begin{aligned} &\left[k_{\text{PI}} w_0 t_{\text{PI}} \cdot (1 + B\zeta) + k_{\text{Si}} w_{\text{Si}} t_{\text{Si}}\right] \frac{\mathrm{d}^2 T}{\mathrm{d}\zeta^2} + (k_{\text{PI}} w_0 t_{\text{PI}} B) \frac{\mathrm{d}T}{\mathrm{d}\zeta} \\ &- \left[2\alpha\ell^2 w_0 (1 + B\zeta)\right] (T - T_{\text{env}}) = 0, \end{aligned} \tag{11}$$

which has the solution

$$\begin{aligned} &T - T_{\text{env}} \\ &= C_1 e^{-b\zeta} \cdot K_M \left[\frac{1}{2}\left(1 - \frac{ab}{B}\right), 1, 2b\left(\zeta + \frac{a+1}{B}\right)\right] \\ &+ C_2 e^{-b\zeta} \cdot K_U \left[\frac{1}{2}\left(1 - \frac{ab}{B}\right), 1, 2b\left(\zeta + \frac{a+1}{B}\right)\right], \end{aligned} \tag{12}$$

where $a = \frac{k_{\text{Si}} w_{\text{Si}} t_{\text{Si}}}{k_{\text{PI}} w_0 t_{\text{PI}}}$ and $b = \ell\sqrt{\frac{2\alpha}{k_{\text{PI}} t_{\text{PI}}}} = \beta\sqrt{a+1}$, C_1 and C_2 are coefficients to be determined from the boundary conditions $T|_{\zeta=0} = T_{\text{h}}$ and $\dot{Q}|_{\zeta=1} = 0$, and K_M and K_U are the Kummer functions (see Appendix A).

Figure 5a shows the temperature distribution for the baseline values, $w_0 = 120\mu$m, and the same material properties as in Section 2; B is fixed at 2, which means the width at the cold side is 3 times of that at the hot side. The temperature distribution is in good agreement with the 3D simulation results obtained by the commercial FEA software ABAQUS, in which the 4-node heat transfer quadrilateral shell elements are employed, with the refined element size that there are at least 8 elements along the thinnest width w_0 of the coil.

Figure 5b presents ΔT and LT_{h} versus the normalized length β for a chosen gradient design of $B = 2$. For the baseline values and $w_0 = 120\mu$m, the gradient width ($B = 2$) gives the maximum power transfer factor $\max(LT_{\text{h}}) = 118.6\mu$W when $\beta = 1.78$. This maximum value is 42% higher than Eq. (7) for the constant width design ($B = 0$) at the baseline values and $w_{\text{PI}} = w_0 = 120\mu$m. This yields the power output 0.22nW (per coil), which is 42% higher than the constant width design, and > 7 times of that in the previous work (0.03nW) [42]. This improvement over the constant width design is mainly due to the increase of PI width (120μm at the hot side and 360μm at the cold side in the gradient width design versus 120μm in the constant width design), which enhances the heat dissipation. This can also be understood from Eq. (7), which shows the linear proportionality to the PI width, though it is limited to the constant width. However, the gradient width design still shows advantage to the constant width design even for the same average width of 240μm, which gives the power output 0.22nW and 0.20nW (per coil), respectively. This advantage of gradient width design is due to the enhanced heat dissipation near the cold side, which improves the local temperature gradient from the constant width design.

Figure 5c shows that the maximum power transfer factor increases linearly with the width gradient B, and is approximately given by

$$\max(LT_{\text{h}}) \approx 0.28 \cdot T_{\text{h}} \cdot \frac{w_{\text{Si}} t_{\text{Si}} k_{\text{Si}}}{\ell_{\text{c}}} \cdot (1 + 0.2B). \tag{13}$$

2.1.3 Discussions

Effect of Coil Geometry on the Power Transfer Efficiency. The power transfer efficiency is defined by the ratio of the converted electric power P_{m} to total heat flux $\dot{Q}_{\text{Si}}$ through the thermoelectric leg, i.e., $\eta = \frac{P_{\text{m}}}{\dot{Q}_{\text{Si}}}$. For a conventional thermoelectric device as shown in Fig. 2b, the power transfer efficiency is independent to its geometric parameters [44] such that the only way to increase the power is to maximize the heat flux [42, 45]. For a thermoelectric coil, however, it depends strongly on the coil geometry. For the simplest case of the coil with a constant width w_{PI} along its length, Eqs. (2) and (3) give the maximum heat flux through the silicon layer from the hot side as

$$\dot{Q}_{\text{Si}} = 2(T_{\text{h}} - T_{\text{env}}) \cdot \frac{k_{\text{Si}} w_{\text{Si}} t_{\text{Si}}}{\ell_{\text{c}}} \cdot \tanh(\beta). \tag{14}$$

With the maximum power given in Eq. (5), the power transfer efficiency is found as

$$\begin{aligned} \eta &= \frac{P_{\text{m}}}{\dot{Q}_{\text{Si}}} \\ &= \frac{1}{4} Z T_{\text{h}} \left(1 - \frac{T_{\text{env}}}{T_{\text{h}}}\right) \cdot \frac{1}{\beta \tanh(\beta)} \left[1 - \frac{1}{\cosh(\beta)}\right]^2, \end{aligned} \tag{15}$$

which clearly depends on the geometry (via β). Therefore, different from the conventional thermoelectric devices, one can not only maximize the heat flux but also optimize the geometry in order to achieve the maximum power. The power transfer efficiency in Eq. (15) reaches its maximum

$$\max(\eta) \approx 0.071 \cdot Z T_{\text{h}} \left(1 - \frac{T_{\text{env}}}{T_{\text{h}}}\right) \tag{16}$$

at $\beta = 2.32$. For Si of $ZT_{\text{h}} \approx 10^{-3}$ under the given boundary condition $T_{\text{h}} = 310$K and $T_{\text{env}} = 291$K, Eq. (16) gives the maximum power efficiency of 4×10^{-6}, which is 60% higher than the previous reported value (2.5×10^{-6}) [42].

Advantage of the Encapsulation PI layer. The low heat transfer coefficient of encapsulation PI layer $k_{\text{PI}} = 0.46$ W/(m$\cdot$K), which is less than 0.6% of that of Si, is undesired for a conventional thermoelectric device because it reduces the heat flux from the hot to the cold sides, therefore limits the thermoelectric power generation. However, the thermoelectric coil takes advantage of the low heat transfer coefficient of the encapsulation PI layer, which serves as a heat sink to cool down the inner Si layer and to generate a large temperature gradient at a small length scale. This is evidenced since the maximum power transfer factor $\max(LT_{\text{h}}) = 83.4\mu$W for the constant width PI layer design is larger than $\max(LT_{\text{h}}) = 62.2\mu$W without the PI layer obtained from Eq. (7), for the baseline values of geometric parameters.

2.2 Mechanical Analysis

The buckling-guided assembly induces bending in the coil, which may lead to brittle fracture in the Si layer. This is governed by the maximum principal strain in Si, where the maximum is with respect to both all directions (at each point) and all points in the Si layer, as given in the following for the flexual-torsional postbuckling of the coil.

2.2.1 Basic Equations

For the undeformed 2D precursor shown in Fig. 6, let $\boldsymbol{E}_i (i = 1,2,3)$ denote the local triad vectors at the centroid line in the orthonormal material frame, where $\boldsymbol{E}_1$ and $\boldsymbol{E}_2$ are along the principal axes of the cross section, and $\boldsymbol{E}_3$ is tangential to the centroid line (Fig. 6). Specifically, direction 1 is in the membrane plane (X-Z plane) and direction 2 is perpendicular to this plane. The curvature of the 2D precursor was defined by Love [46] as

$$\frac{d\boldsymbol{E}_i}{dS} = \boldsymbol{K} \times \boldsymbol{E}_i \ (i = 1,2,3), \tag{17}$$

where S is the arc-length coordinate and $\boldsymbol{K} = K_1 \boldsymbol{E}_1$ is the curvature of the 2D precursor in the initial, undeformed configuration, with $K_1 = 1/R$ for $S \in [0, \pi R)$ and $K_1 = -1/R$ for $S \in [\pi R, 2\pi R]$. The triad vectors $\boldsymbol{E}_i (i = 1,2,3)$ move to $\boldsymbol{e}_i (i = 1,2,3)$ during deformation. The curvature $\hat{\boldsymbol{\kappa}}$ of the deformed 3D coil is similarly defined by

$$\frac{d\boldsymbol{e}_i}{ds} = \hat{\boldsymbol{\kappa}} \times \boldsymbol{e}_i \ (i = 1,2,3), \tag{18}$$

where s is the arc-length coordinate in the deformed configuration, and $\hat{\boldsymbol{\kappa}} = \hat{\kappa}_i \boldsymbol{e}_i$, with the bending curvatures $\hat{\kappa}_1$ and $\hat{\kappa}_2$, and the twisting curvature $\hat{\kappa}_3$. The elongation of the deformed coil is

$$\lambda = \frac{ds}{dS}. \tag{19}$$

For linear elastic and isotropic materials, the axial force t_3, bending moments m_1 and m_2, and torque m_3 are related to the above stretch and curvatures by

$$\begin{aligned} t_3 &= D_0(\lambda - 1), \\ m_1 &= D_1(\hat{\kappa}_1 - K_1), \\ m_2 &= D_2 \hat{\kappa}_2, \\ m_3 &= D_{\text{T}} \hat{\kappa}_3, \end{aligned} \tag{20}$$

where D_0 is the tensile stiffness, $D_i \ (i = 1,2)$ are the bending stiffnesses, and D_{T} is the torsional stiffness. For the PI-Si-PI composite thin-film beam illustrated in Fig. 1, they are given by

$$\begin{aligned} D_0^{(\text{c})} &= E_{\text{Si}} w_{\text{Si}} t_{\text{Si}} + E_{\text{PI}} w_{\text{PI}} t_{\text{PI}}, \\ D_1^{(\text{c})} &= \frac{1}{12} E_{\text{Si}} w_{\text{Si}}^3 t_{\text{Si}} + \frac{1}{12} E_{\text{PI}} w_{\text{PI}}^3 t_{\text{PI}}, \\ D_2^{(\text{c})} &= \frac{1}{12} (E_{\text{Si}} - E_{\text{PI}}) w_{\text{Si}} t_{\text{Si}}^3 + \frac{1}{12} E_{\text{PI}} w_{\text{PI}} (t_{\text{Si}} + t_{\text{PI}})^3 \\ &\quad + \frac{1}{12} E_{\text{PI}} (w_{\text{PI}} - w_{\text{Si}}) t_{\text{PI}}^3, \\ D_{\text{T}}^{(\text{c})} &= \frac{E_{\text{PI}}}{6(1+\nu_{\text{PI}})} \left[\left(1 - 0.63 \frac{t_{\text{PI}}}{w_{\text{PI}}}\right) w_{\text{PI}} t_{\text{PI}}^3 + \right. \\ &\quad \left(1 - 0.63 \frac{t_{\text{PI}} + t_{\text{Si}}}{w_{\text{Si}}}\right) w_{\text{Si}} (t_{\text{PI}} + t_{\text{Si}})^3 \\ &\quad \left. - \left(1 - 0.63 \frac{t_{\text{PI}}}{w_{\text{Si}}}\right) w_{\text{Si}} t_{\text{PI}}^3 - \left(1 - 0.63 \frac{t_{\text{Si}}}{w_{\text{Si}}}\right) w_{\text{Si}} t_{\text{Si}}^3 \right] \\ &\quad + \frac{E_{\text{Si}}}{6(1+\nu_{\text{Si}})} \left[\left(1 - 0.63 \frac{t_{\text{Si}}}{w_{\text{Si}}}\right) w_{\text{Si}} t_{\text{Si}}^3 \right], \end{aligned} \tag{21}$$

where $E_{\text{PI}} = 2.5$GPa and $E_{\text{Si}} = 130$GPa are the elastic moduli of PI and Si, respectively, and $\nu_{\text{PI}} = 0.34$ and $\nu_{\text{Si}} = 0.27$ are the Poisson's ratios.

Without any distributed forces or moments, the internal forces ($\boldsymbol{t} = t_i \boldsymbol{e}_i$) and moments ($\boldsymbol{m} = m_i \boldsymbol{e}_i$) in the coil satisfy the static equilibrium [29],

$$\frac{d\boldsymbol{t}}{dS} = 0, \tag{22}$$

$$\frac{d\boldsymbol{m}}{dS} + \lambda \boldsymbol{e}_3 \times \boldsymbol{t} = 0. \tag{23}$$

The boundary conditions are

$$\begin{aligned} U_X|_{A,B} = U_Y|_{A,B} = 0, \ \boldsymbol{e}_i|_{A,B} = \boldsymbol{E}_i|_{A,B}, \\ U_Z|_A = \frac{U_{\text{app}}}{2}, \ U_Z|_B = -\frac{U_{\text{app}}}{2}, \end{aligned} \tag{24}$$

where $U_{X,Y,Z}|_{A,B}$ are displacements in the X, Y and Z directions at the two ends A and B of the 2D precursor, respectively (see Fig. 6), and U_{app} is the applied displacement between A and B and is given by

$$U_{\text{app}} = 4R \cdot \varepsilon_{\text{app}}. \tag{25}$$

Here $4R$ is the distance between the two ends A and B, and the applied compressive strain ε_{app} is related to the prestrain ε_{pre} by

$$\varepsilon_{\text{app}} = \frac{\varepsilon_{\text{pre}}}{1+\varepsilon_{\text{pre}}}. \tag{26}$$

2.2.2 Analysis for a Uniform Thin Beam

We first consider a curved ribbon with a thin, rectangular cross section of a single material, which paves the way for the analysis in the next section for a PI-Si-PI cross section. For the thickness t much smaller than the width w, Fan et al. [29, 47] obtained the maximum principal strain at the midpoint of the long edge (w) of the cross section as

$$\varepsilon_{\text{edge}} = t\left(\frac{1-\nu}{4}\left|\hat{\kappa}_2\right| + \frac{1}{2}\sqrt{\frac{(1+\nu)^2}{4}\hat{\kappa}_2 + \hat{\kappa}_3^2}\right), \tag{27}$$

where ν is the Poisson's ratio of the material, and the curvatures scale with the square root of the applied strain [29], i.e.,

$$\left(\hat{\kappa}_1 - K_1, \hat{\kappa}_2, \hat{\kappa}_3\right) \sim \frac{1}{R}\sqrt{\frac{\varepsilon_{\text{pre}}}{1+\varepsilon_{\text{pre}}}}. \tag{28}$$

Equation (28) holds for the negligible elongation ($\lambda - 1$). The maximum principal strain at the corner of the rectangular cross section results from bending in both directions as

$$\varepsilon_{\text{corner}} = t\left(\frac{1}{2}\left|\hat{\kappa}_2\right| + \frac{1}{2}\frac{w}{t}\left|\hat{\kappa}_1 - K_1\right|\right). \tag{29}$$

The maximum principal strain in the ribbon, along the length and across the section, is

$$\varepsilon_{\max} = \max\left(\varepsilon_{\text{edge}}, \varepsilon_{\text{corner}}\right). \tag{30}$$

Liu et al. [48] reported that the curvatures $\hat{\kappa}_1$ and $\hat{\kappa}_2$ follow the scaling law

$$\left|\hat{\kappa}_1 - K_1\right| \sim \frac{D_2}{D_1}\left|\hat{\kappa}_2\right|. \tag{31}$$

Its substitution into Eq. (29), together with Eq. (27), (28) and (30), yield the scaling law for the overall maximum strain as

$$\varepsilon_{\max} \sim \frac{t}{R}\sqrt{\frac{\varepsilon_{\text{pre}}}{1+\varepsilon_{\text{pre}}}}\left(c_1 + c_2\frac{D_2}{D_1}\frac{w}{t}\right). \tag{32}$$

where c_1 and c_2 are constants to be determined.

2.2.3 Analysis for a Composite Thin Beam

For the coil with composite PI-Si-PI layer, the scaling law in Eq. (32) still holds for Si except that the thickness of the Si layer and the composite bending stiffness in Eq. (21) should be used instead, i.e.,

$$\varepsilon_{\max} \sim \frac{t_{\text{Si}}}{R}\sqrt{\frac{\varepsilon_{\text{pre}}}{1+\varepsilon_{\text{pre}}}}\left(c_1 + c_2\frac{D_2^{(c)}}{D_1^{(c)}}\frac{w_{\text{Si}}}{t_{\text{Si}}}\right). \tag{33}$$

FEA is conducted for more than 150 combinations of the seven material and geometric parameters (E_{PI}, E_{Si}, w_{PI}, w_{Si}, t_{PI}, t_{Si} and R) and prestrain ε_{pre}, as shown in Fig. 7, and each of these 8 parameters varies independently. The commercial software ABAQUS is used, with the eight-node quadratic shell elements and the refined mesh to ensure accuracy. The normalized maximum strain $\varepsilon_{\max}\frac{R}{t_{\text{Si}}}\sqrt{\frac{1+\varepsilon_{\text{pre}}}{\varepsilon_{\text{pre}}}}$ agrees well with Eq. (33) for the parameters $c_1 = 0.8$ and $c_2 = 0.6$. For the baseline values of the parameters, the maximum principal strain in the Si layer is 0.030% which is far smaller than the fracture strain (i.e., 0.1%) [43].

For the gradient PI width, Fig. 8 shows that the normalized maximum principal strain in the Si layer increases linearly with the PI width gradient B. Accordingly Eq. (31) is modified as

$$\varepsilon_{\max} = \frac{t_{\text{Si}}}{R}\sqrt{\frac{\varepsilon_{\text{pre}}}{1+\varepsilon_{\text{pre}}}}\left(0.8 + 0.6\frac{D_2^{(c)}}{D_1^{(c)}}\frac{w_{\text{Si}}}{t_{\text{Si}}}\right)(1+0.35B), \tag{34}$$

It should be pointed out that, even though the PI width gradient B increases the efficiency of thermoelectric power generation as discussed in Section 2.1.2, it also increases the maximum strain in the Si layer therefore reduces its mechanical robustness. For example, for a coil of gradient width design with baseline geometric values ($w_0 = 60\mu$m) and width gradient $B = 3$, the maximum strain in the Si layer is $> 0.06\%$ which is twice higher than the constant width design. Therefore, the PI width gradient B needs to be properly chosen in this competition between the efficient of thermoelectric power generation and mechanical robustness.

3 Conclusion

Systematic studies of key effects of geometric and parameters on the thermoelectric and mechanical properties reveal design strategies for the thermoelectric coils as fabricated by buckling-guided 3D assembly technique. Thermal analysis significantly improves the maximum thermoelectric power output of a coil compared to the previous work (0.03nW) [42], i.e., by 5 times with the uniform PI width design and 7 times with the gradient PI width design. This thermoelectric model, which is applicable to similar ribbon- or fiber- like thermoelectric devices [45,49,50], demonstrates the huge improvement space of such device and a promising future. Mechanical analysis reveals the importance of in-plane bending in the thermoelectric coil which was ignored in the previous works on the post-buckling behaviors of a thin-film ribbon, and provides a prediction of the maximum strain in the Si layer of the coil with composite PI-Si-PI layer. The safety of the brittle Si layer as well as the mechanical robustness of the coil are therefore ensured for future applications.

References

[1] Pikul, J. H., Zhang, H. G., Cho, J., Braun, P. V., and King, W. P., 2013. “High-power lithium ion microbatteries from interdigitated three-dimensional bicontinuous nanoporous electrodes”. *Nature communications,* **4**(1), pp. 1–5.

[2] Sun, K., Wei, T.-S., Ahn, B. Y., Seo, J. Y., Dillon, S. J., and Lewis, J. A., 2013. “3d printing of interdigitated li-ion microbattery architectures”. *Advanced materials,* **25**(33), pp. 4539–4543.

[3] Han, M., Wang, H., Yang, Y., Liang, C., Bai, W., Yan, Z., Li, H., Xue, Y., Wang, X., Akar, B., et al., 2019. “Three-dimensional piezoelectric polymer microsystems for vibrational energy harvesting, robotic interfaces and biomedical implants”. *Nature Electronics,* **2**(1), pp. 26–35.

[4] Zheng, X., Lee, H., Weisgraber, T. H., Shusteff, M., DeOtte, J., Duoss, E. B., Kuntz, J. D., Biener, M. M., Ge, Q., Jackson, J. A., et al., 2014. “Ultralight, ultrastiff mechanical metamaterials”. *Science,* **344**(6190), pp. 1373–1377.

[5] Liu, Z., Du, H., Li, J., Lu, L., Li, Z.-Y., and Fang, N. X., 2018. “Nano-kirigami with giant optical chirality”. *Science advances,* **4**(7), p. eaat4436.

[6] Yan, D., Chang, J., Zhang, H., Liu, J., Song, H., Xue, Z., Zhang, F., and Zhang, Y., 2020. “Soft three-dimensional network materials with rational biomimetic designs”. *Nature communications,* **11**(1), pp. 1–11.

[7] Jang, K.-I., Li, K., Chung, H. U., Xu, S., Jung, H. N., Yang, Y., Kwak, J. W., Jung, H. H., Song, J., Yang, C., et al., 2017. “Self-assembled three dimensional network designs for soft electronics”. *Nature communications,* **8**(1), pp. 1–10.

[8] Li, K., Cheng, X., Zhu, F., Li, L., Xie, Z., Luan, H., Wang, Z., Ji, Z., Wang, H., Liu, F., et al., 2019. “A generic soft encapsulation strategy for stretchable electronics”. *Advanced Functional Materials,* **29**(8), p. 1806630.

[9] Ma, Q., and Zhang, Y., 2016. “Mechanics of fractal-inspired horseshoe microstructures for applications in stretchable electronics”. *Journal of Applied Mechanics,* **83**(11).

[10] Pang, W., Cheng, X., Zhao, H., Guo, X., Ji, Z., Li, G., Liang, Y., Xue, Z., Song, H., Zhang, F., et al., 2020. “Electro-mechanically controlled assembly of reconfigurable 3d mesostructures and electronic devices based on dielectric elastomer platforms”. *National Science Review,* **7**(2), pp. 342–354.

[11] Lind, J. U., Busbee, T. A., Valentine, A. D., Pasqualini, F. S., Yuan, H., Yadid, M., Park, S.-J., Kotikian, A., Nesmith, A. P., Campbell, P. H., et al., 2017. “Instrumented cardiac microphysiological devices via multimaterial three-dimensional printing”. *Nature materials,* **16**(3), pp. 303–308.

[12] Bolaños Quiñones, V. A., Zhu, H., Solovev, A. A., Mei, Y., and Gracias, D. H., 2018. “Origami biosystems: 3d assembly methods for biomedical applications”. *Advanced Biosystems,* **2**(12), p. 1800230.

[13] Zhu, W., Li, J., Leong, Y. J., Rozen, I., Qu, X., Dong, R., Wu, Z., Gao, W., Chung, P. H., Wang, J., et al., 2015. “3d-printed artificial microfish”. *Advanced materials,* **27**(30), pp. 4411–4417.

[14] Truby, R. L., and Lewis, J. A., 2016. “Printing soft matter in three dimensions”. *Nature,* **540**(7633), pp. 371–378.

[15] Skylar-Scott, M. A., Gunasekaran, S., and Lewis, J. A., 2016. “Laser-assisted direct ink writing of planar and 3d metal architectures”. *Proceedings of the National Academy of Sciences,* **113**(22), pp. 6137–6142.

[16] Zhang, Y., Zhang, F., Yan, Z., Ma, Q., Li, X., Huang, Y., and Rogers, J. A., 2017. “Printing, folding and assembly methods for forming 3d mesostructures in advanced materials”. *Nature Reviews Materials,* **2**(4), pp. 1–17.

[17] Shenoy, V. B., and Gracias, D. H., 2012. “Self-folding thin-film materials: From nanopolyhedra to graphene origami”. *Mrs Bulletin,* **37**(9), p. 847.

[18] Chen, Z., Huang, G., Trase, I., Han, X., and Mei, Y., 2016. “Mechanical self-assembly of a strain-engineered flexible layer: wrinkling, rolling, and twisting”. *Physical Review Applied,* **5**(1), p. 017001.

[19] Cui, J., Yao, S., Huang, Q., Adams, J. G., and Zhu, Y., 2017. “Controlling the self-folding of a polymer sheet using a local heater: the effect of the polymer–heater interface”. *Soft Matter,* **13**(21), pp. 3863–3870.

[20] Ware, T. H., McConney, M. E., Wie, J. J., Tondiglia, V. P., and White, T. J., 2015. “Voxelated liquid crystal elastomers”. *Science,* **347**(6225), pp. 982–984.

[21] Yoon, C., Xiao, R., Park, J., Cha, J., Nguyen, T. D., and Gracias, D. H., 2014. “Functional stimuli responsive hydrogel devices by self-folding”. *Smart Materials and Structures,* **23**(9), p. 094008.

[22] Xia, Y., Cedillo-Servin, G., Kamien, R. D., and Yang, S., 2016. “Guided folding of nematic liquid crystal elastomer sheets into 3d via patterned 1d microchannels”. *Advanced Materials,* **28**(43), pp. 9637–9643.

[23] Xu, S., Yan, Z., Jang, K.-I., Huang, W., Fu, H., Kim, J., Wei, Z., Flavin, M., McCracken, J., Wang, R., et al., 2015. “Assembly of micro/nanomaterials into complex, three-dimensional architectures by compressive buckling”. *Science,* **347**(6218), pp. 154–159.

[24] Zhang, Y., Yan, Z., Nan, K., Xiao, D., Liu, Y., Luan, H., Fu, H., Wang, X., Yang, Q., Wang, J., et al., 2015. “A mechanically driven form of kirigami as a route to 3d mesostructures in micro/nanomembranes”. *Proceedings of the National Academy of Sciences,* **112**(38), pp. 11757–11764.

[25] Yan, Z., Zhang, F., Liu, F., Han, M., Ou, D., Liu, Y., Lin, Q., Guo, X., Fu, H., Xie, Z., et al., 2016. "Mechanical assembly of complex, 3d mesostructures from releasable multilayers of advanced materials". *Science advances,* **2**(9), p. e1601014.

[26] Yan, Z., Zhang, F., Wang, J., Liu, F., Guo, X., Nan, K., Lin, Q., Gao, M., Xiao, D., Shi, Y., et al., 2016. "Controlled mechanical buckling for origami-inspired construction of 3d microstructures in advanced materials". *Advanced functional materials,* **26**(16), pp. 2629–2639.

[27] Nan, K., Luan, H., Yan, Z., Ning, X., Wang, Y., Wang, A., Wang, J., Han, M., Chang, M., Li, K., et al., 2017. "Engineered elastomer substrates for guided assembly of complex 3d mesostructures by spatially nonuniform compressive buckling". *Advanced functional materials,* **27**(1), p. 1604281.

[28] Yan, Z., Han, M., Shi, Y., Badea, A., Yang, Y., Kulkarni, A., Hanson, E., Kandel, M. E., Wen, X., Zhang, F., et al., 2017. "Three-dimensional mesostructures as high-temperature growth templates, electronic cellular scaffolds, and self-propelled microrobots". *Proceedings of the National Academy of Sciences,* **114**(45), pp. E9455–E9464.

[29] Fan, Z., Hwang, K.-C., Rogers, J. A., Huang, Y., and Zhang, Y., 2018. "A double perturbation method of postbuckling analysis in 2d curved beams for assembly of 3d ribbon-shaped structures". *Journal of the Mechanics and Physics of Solids,* **111**, pp. 215–238.

[30] Zhao, H., Li, K., Han, M., Zhu, F., Vázquez-Guardado, A., Guo, P., Xie, Z., Park, Y., Chen, L., Wang, X., et al., 2019. "Buckling and twisting of advanced materials into morphable 3d mesostructures". *Proceedings of the National Academy of Sciences,* **116**(27), pp. 13239–13248.

[31] Xu, Z., Fan, Z., Zi, Y., Zhang, Y., and Huang, Y., 2020. "An inverse design method of buckling-guided assembly for ribbon-type 3d structures". *Journal of Applied Mechanics,* **87**(3).

[32] Yan, Z., Wang, B., Wang, K., Zhao, S., Li, S., Huang, Y., and Wang, H., 2020. "Cellular substrate to facilitate global buckling of serpentine structures". *Journal of Applied Mechanics,* **87**(2).

[33] Feng, P., Yuan, J., Huang, Y., and Li, X., 2020. "Analytical solutions for the lateral-torsional buckling of serpentine interconnects in stretchable electronics". *Journal of Applied Mechanics,* **87**(8).

[34] Tang, R., and Fu, H., 2020. "Mechanics of buckled kirigami membranes for stretchable interconnects in island-bridge structures". *Journal of Applied Mechanics,* **87**(5).

[35] Zhao, S., Zhu, F., Yan, Z., Li, D., Xiang, J., Huang, Y., and Luan, H., 2020. "A nonlinear mechanics model of zigzag cellular substrates for stretchable electronics". *Journal of Applied Mechanics,* **87**(6).

[36] Liu, S., Ha, T., and Lu, N., 2019. "Experimentally and numerically validated analytical solutions to nonbuckling piezoelectric serpentine ribbons". *Journal of Applied Mechanics,* **86**(5).

[37] Huang, Y., Mu, Z., Feng, P., and Yuan, J., 2019. "Mechanics design for compatible deformation of fractal serpentine interconnects in high-density stretchable electronics". *Journal of Applied Mechanics,* **86**(3).

[38] Zhao, J., Zhang, Y., Li, X., and Shi, M., 2019. "An improved design of the substrate of stretchable gallium arsenide photovoltaics". *Journal of Applied Mechanics,* **86**(3).

[39] Liu, G., Sun, L., and Su, Y., 2020. "Scaling effects in the mechanical system of the flexible epidermal electronics and the human skin". *Journal of Applied Mechanics,* **87**(8).

[40] Yin, S., and Su, Y., 2019. "A traction-free model for the tensile stiffness and bending stiffness of laminated ribbons of flexible electronics". *Journal of Applied Mechanics,* **86**(5).

[41] He, W., Zhang, G., Zhang, X., Ji, J., Li, G., and Zhao, X., 2015. "Recent development and application of thermoelectric generator and cooler". *Applied Energy,* **143**, pp. 1–25.

[42] Nan, K., Kang, S. D., Li, K., Yu, K. J., Zhu, F., Wang, J., Dunn, A. C., Zhou, C., Xie, Z., Agne, M. T., et al., 2018. "Compliant and stretchable thermoelectric coils for energy harvesting in miniature flexible devices". *Science advances,* **4**(11), p. eaau5849.

[43] Vedde, J., and Gravesen, P., 1996. "The fracture strength of nitrogen doped silicon wafers". *Materials Science and Engineering: B,* **36**(1-3), pp. 246–250.

[44] Hadjistassou, C., Kyriakides, E., and Georgiou, J., 2013. "Designing high efficiency segmented thermoelectric generators". *Energy conversion and management,* **66**, pp. 165–172.

[45] Sun, T., Zhou, B., Zheng, Q., Wang, L., Jiang, W., and Snyder, G. J., 2020. "Stretchable fabric generates electric power from woven thermoelectric fibers". *Nature communications,* **11**(1), pp. 1–10.

[46] Love, A., 1927. "A treatise on the mathematical theory of elasticity, 4th edn new york". *NY: Dover.[Google Scholar].*

[47] Fan, Z., Wu, J., Ma, Q., Liu, Y., Su, Y., and Hwang, K.-C., 2017. "Post-buckling analysis of curved beams". *Journal of Applied Mechanics,* **84**(3).

[48] Liu, L., and Lu, N., 2016. "Variational formulations, instabilities and critical loadings of space curved beams". *International Journal of Solids and Structures,* **87**, pp. 48–60.

[49] Yadav, A., Pipe, K., and Shtein, M., 2008. "Fiber-based flexible thermoelectric power generator". *Journal of Power Sources,* **175**(2), pp. 909–913.

[50] Zhang, T., Li, K., Zhang, J., Chen, M., Wang, Z., Ma, S., Zhang, N., and Wei, L., 2017. "High-performance, flexible, and ultralong crystalline thermoelectric fibers". *Nano Energy,* **41**, pp. 35–42.

[51] Kummer, E. E., 1837. "De integralibus quibusdam definitis et seriebus infinitis.". *Journal für die reine und angewandte Mathematik,* **1837**(17), pp. 228–242.

Appendix: Kummer Functions

The Kummer functions $K_M(a,b,z)$ and $K_U(a,b,z)$ are defined by [51]

$$K_M(a,b,z) = \frac{\Gamma(b)}{\Gamma(a)} \sum_{n=0}^{\infty} \frac{\Gamma(n+a)}{n!\Gamma(n+b)} z^n \tag{35}$$

and

$$\begin{aligned} K_U(a,b,z) = \frac{\pi}{\sin(\pi b)} \Bigg[& \frac{K_M(a,b,z)}{\Gamma(b)\Gamma(a-b+1)} \\ & -z^{(1-b)} \frac{K_M(a-b+1,2-b,z)}{\Gamma(a)\Gamma(2-b)} \Bigg] \end{aligned} \tag{36}$$

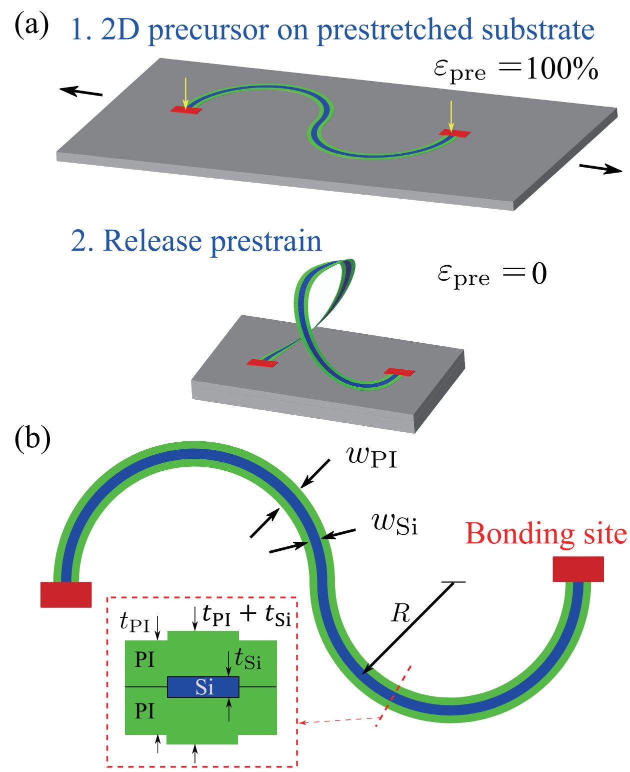

Fig. 1. (a) Buckling-guided assembly of coils, which undergoes two steps of fabrication: Selectively bond the 2D precursor onto the prestretched substrate at the bonding sites; release the prestrain and the 2D precursor pops-up into the 3D configuration by compressive buckling. (b) Geometry of the 2D precursor.

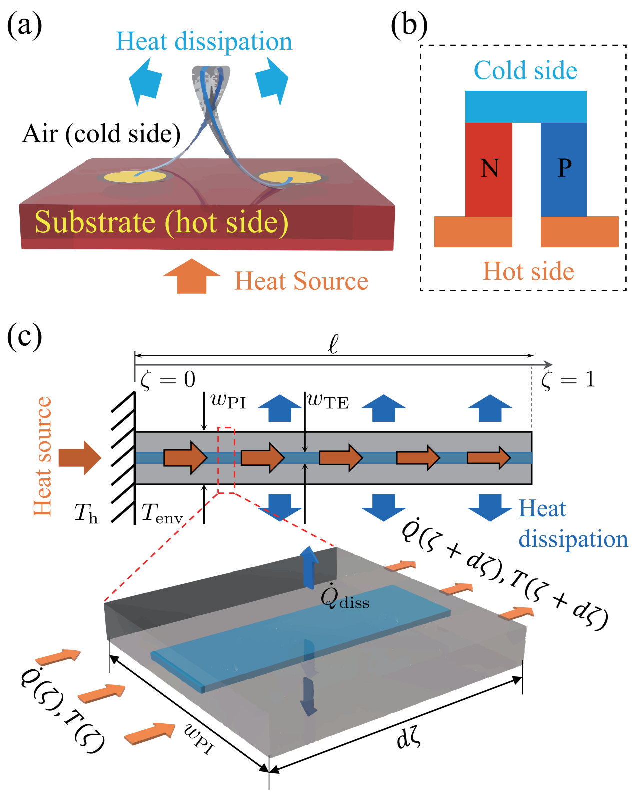

Fig. 2. The analytical heat-transfer model for thin-film coil. (a) Heat transfer for a coil on the hot substrate. (b) Schematic illustration of the conventional thermoelectric device. (c) Simplified analytic heat-transfer model for a composite thin film coil.

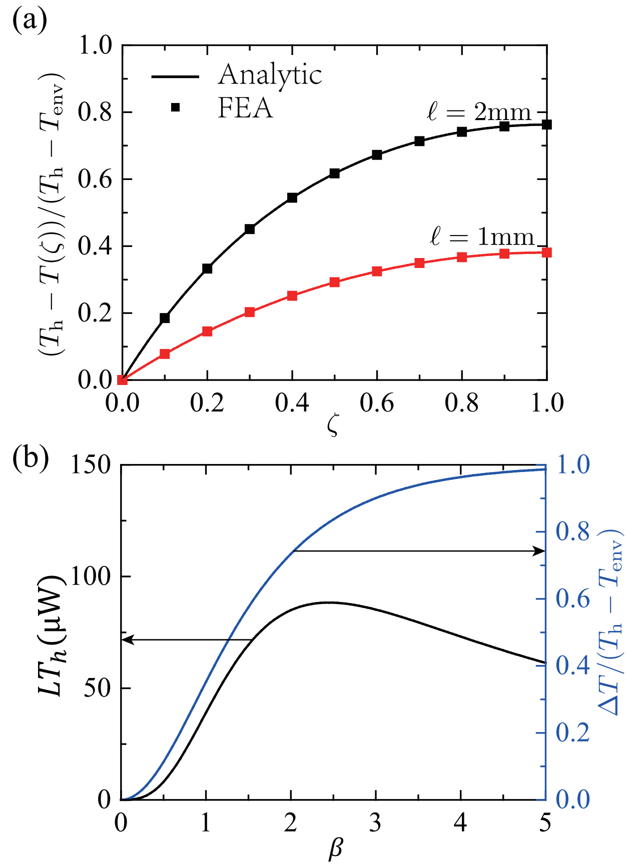

Fig. 3. Thermal analysis for the coil of constant width. (a) The temperature distribution in a ribbon from the hottest side ($\zeta = 0$) to the coldest side ($\zeta = 1$). The dots represent the FEA results, and the curves represent the analytic model. (b) Largest temperature drop and the power output coefficient LT_{h} versus the normalized ribbon length β. The hot-side temperature is $T_{\mathrm{h}} = 310\mathrm{K}$.

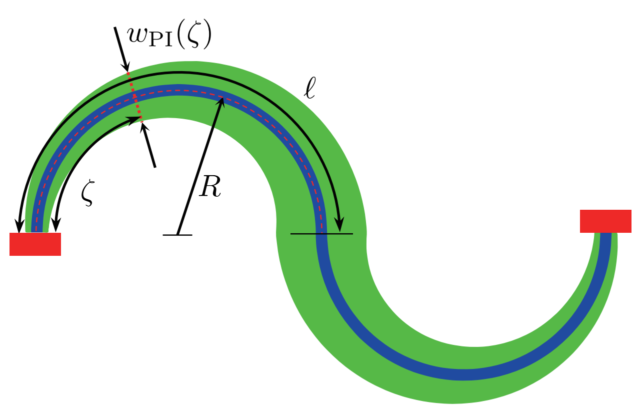

Fig. 4. Geometry of the 2D precursor with gradient PI width.

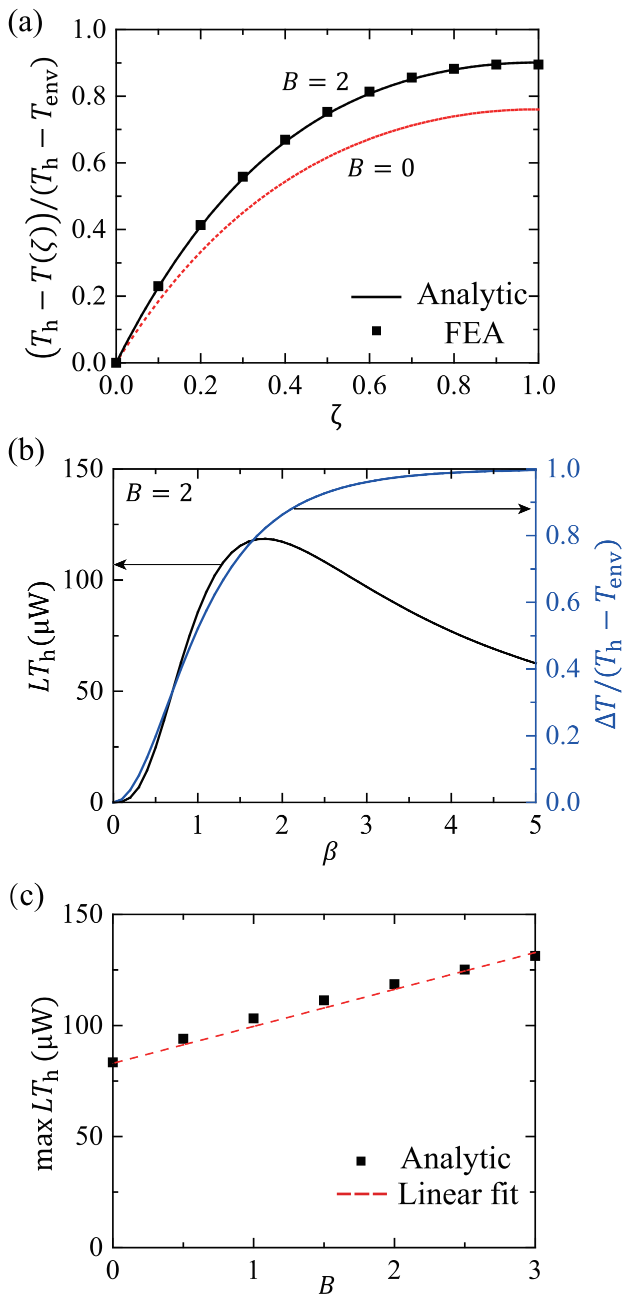

Fig. 5. Thermal analysis for the coil with gradient PI width. (a) Normalized temperature distribution from $\zeta = 0$ to 1, for $B = 0$ and 2 and chosen $\ell = 2\text{mm}$. The dots represent the FEA results, and the curves represent the analytic model. (b) The power output coefficient LT_{h} and the hottest-to-coldest temperature drop ΔT versus the normalized ribbon length β for a gradient width design with $B = 2$. The hot-side temperature is $T_{\text{h}} = 310\text{K}$. (c) The maximum value of LT_{h} versus the PI layer width gradient B.

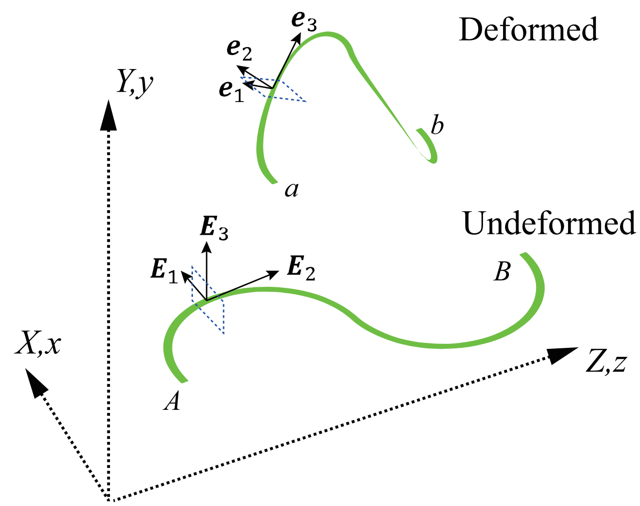

Fig. 6. Schematic illustration of the undeformed and deformed curved ribbon.

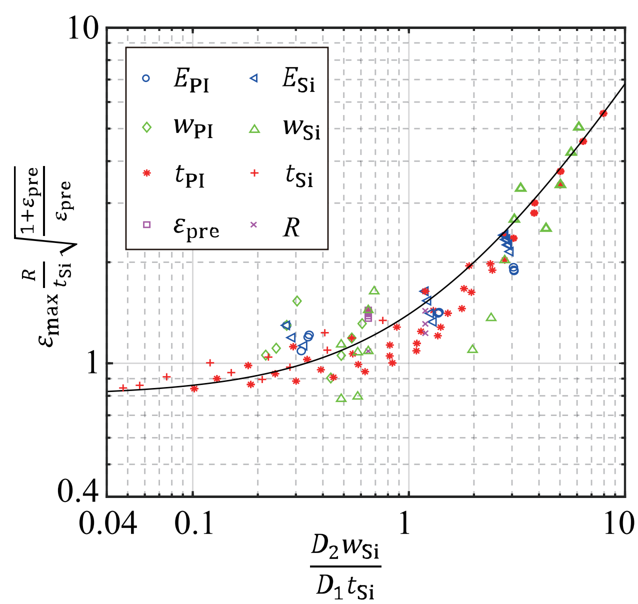

Fig. 7. Scaling law for the normalized maximum strain in Si layer in the design space $E_{\text{PI}}, E_{\text{Si}} \in [2.5, 130]\text{GPa}$, $t_{\text{PI}} \in [1, 10]\mu\text{m}$, $t_{\text{Si}} \in [0.2, 1]\mu\text{m}$, $w_{\text{PI}} \in [100, 140]\mu\text{m}$, $w_{\text{Si}} \in [30, 80]\mu\text{m}$, $R \in [300, 800]\mu\text{m}$, $\varepsilon_{\text{pre}} \in [0.5, 1.0]$. Each parameter varies independently from the baseline values.

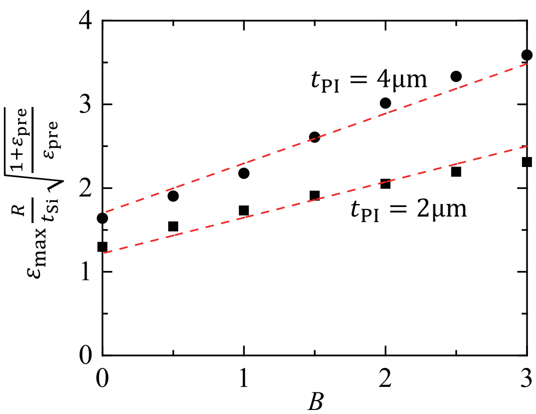

Fig. 8. Normalized maximum strain in Si layer versus the PI width gradient for the coil of gradient width design.